The reconstruction of the surface is not completed for the coverage of 0.33 ML Fe. Well-ordered islands are separated by areas, where the atoms display merely short-range ordering similar to that observed after annealing at 250°C (Fig. 1). All characteristic features i.e. three atoms rings with the distance between member atoms equal to 6.6 Å, random positions of rings on the surface and their identical azimuthal orientation are found after annealing at 400°C. The amount of three atoms rings is substantially higher in comparison with treatment at lower temperature. The surface of ordered islands, several nanometers in size, is terminated with identically imaged by STM atoms aligned in hexagonal, closely packed structure. The nearest neighbour distance, equal to 7.6 Å, corresponds to 2×2 reconstruction of CsCl- or CaF_2-type phase of iron silicide. The islands, which usually have non-regular shape, are located randomly on the substrate surface. The same azimuthal orientation of all islands proves their epitaxial growth on Si surface.

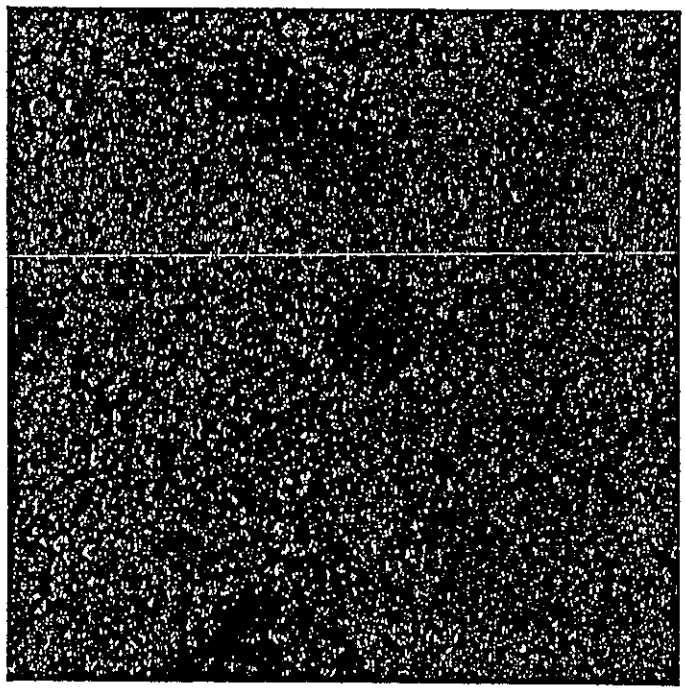

Fig. 1. Partial 2×2 reconstruction upon deposition of 0.33 ML Fe and annealing at 400°C (37.5×37.5 nm^2).

Deposition of 2 ML of Fe annealed subsequently at 400°C, on the contrary to the discussed above case, results in complete surface ordering. Large scan STM image (Fig. 2) shows three entirely reconstructed terraces of Si vicinal substrate. The roughness of each terrace is very low — regular in shapes, atomically flat areas are confined by borders oriented every 60°, determined by the rows of atoms. The fluctuation of the surface profile within the same terrace does not exceed one monolayer. Figure 3a shows a high resolution STM topography image of a single

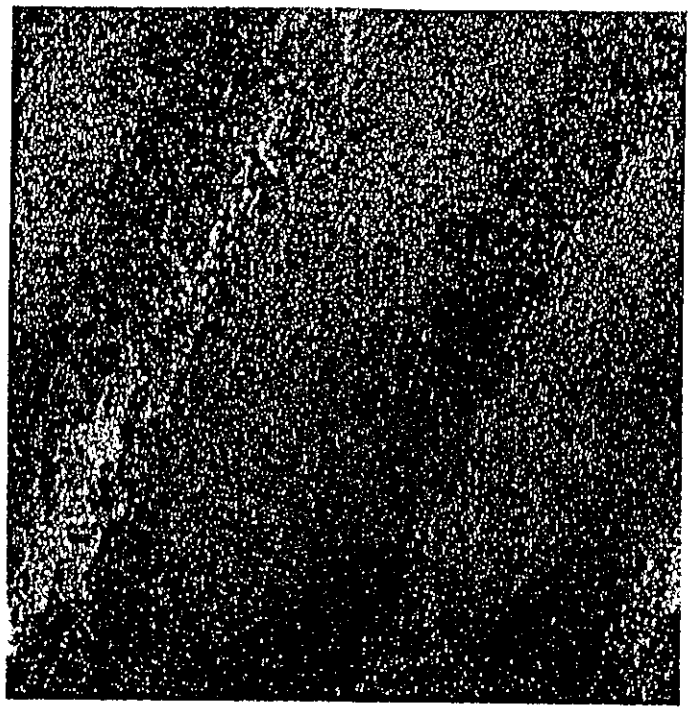

Fig. 2. The topography image with derivative component (200 × 200 nm^2) of entirely reconstructed vicinal surface covered with 2 ML Fe and annealed at 400°C.

terrace. The image was recorded at negative bias, for which the occupied states were probed. Three terminating atomic planes are clearly distinguished. The STM image of surface atoms differs depending on the plane. In the lowest layer every atom seems to be identical. In the middle plane some atoms are seen as the "lower" ones (for further discussion they are assumed to be of A-type, whereas the others — as B-type). As discussed in the next part of the paper, variation in apparent height of surface atoms imaged by STM is associated merely with spectroscopic effects, which suggest that their electronic structures differ. Atoms, imaged as "lower", are in minority and their population is estimated on the level of 12%. Their distribution in plane is random, without any tendency to agglomerate in clusters. In the highest plane the contribution of A-type and B-type atoms is comparable, therefore it frequently happens that two or more atoms of the same type neighbour each other. The surface profile (Fig. 3b) enables unambiguous differentiation of two types of atoms. The height of terrace steps, equal to 1.5 Å, favours CsCl-type structure of iron silicide over CaF_2-type, for which the terrace step height is expected to be equal to 3.1 Å [2]. On this basis one may infer that all atoms in the lowest plane are of B-type, which type appears also in majority in the middle terrace and finally in comparable amount to A-type atoms in the highest plane. The distribution trend of both types of atoms on the surface — the higher terrace the higher concentration of A-type atoms — is very clear. For negative bias A-type atoms are imaged as "lower", as mentioned previously, by 0.6 Å.

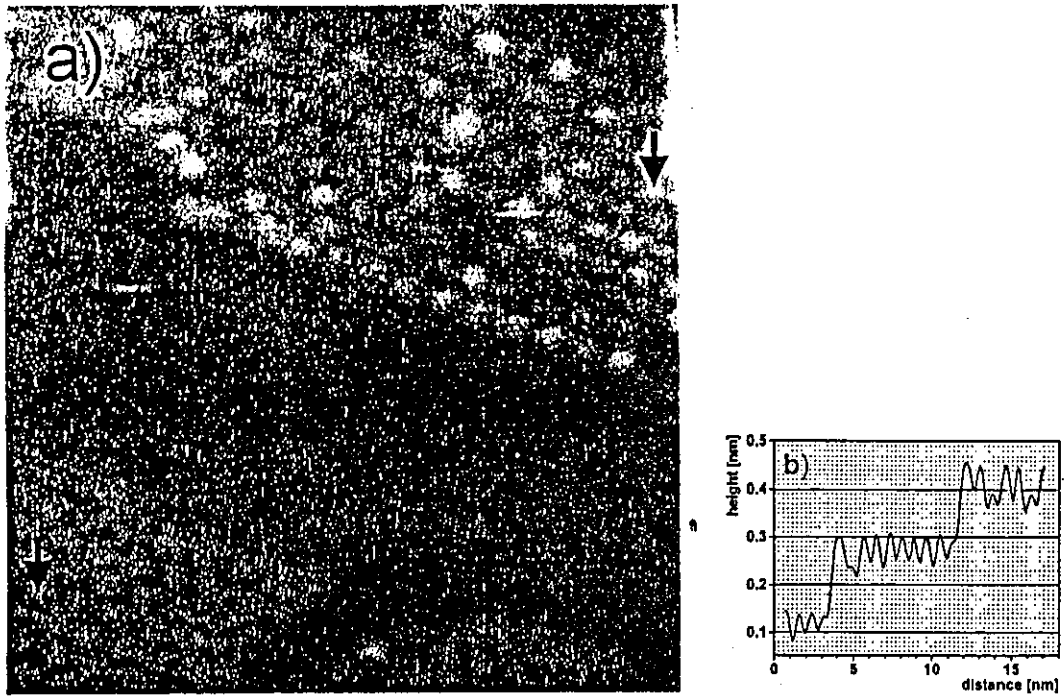

Fig. 3. (a) Recorded at –1.93 V STM image (15×15 nm^2) of a single vicinal terrace after deposition of 2 ML Fe and subsequent annealing at 400°C. The content of atoms imaged as "lower" (A-type) depends on the terminating atomic plane with a tendency: higher plane–higher contribution, (b) the surface profile measured between arrows.

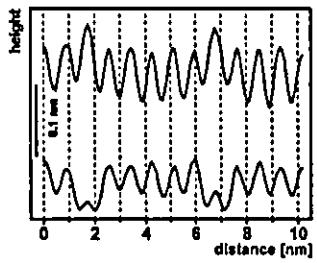

Fig. 4. Corrugation profile of the same row of atoms taken at +1.9 V (upper) and –1.9 V (bottom).

Typical variation of the atom imaging by STM is quantitatively depicted in Fig. 4, which shows two corrugation profiles along the row of atoms, containing both A and B types, measured at various biases. In the upper profile, where the empty states are probed, the apparent height of A-type atoms is larger by 0.2 Å relatively to B-type ones. The opposite bias inverts the STM image — the A-type atoms are probed as "lower", approximately by 0.4 Å in comparison to B-type ones. The neighbourhood of different in type atoms does not seem to affect the way of imaging. As seen in the profile, B-type atoms adjacent to A-type have the same apparent height as these in the uniform row of B-type atoms. The above lack

of neighbourhood influence may be a consequence of weak interaction in plane resulting from the large separation distance and/or a strong localization of electronic states. Also the absence of lateral shift position of atoms imaged at opposite biases suggests the lack of spatial separation of empty and occupied states.

The annealing at higher temperature activates entirely different growth mode of iron silicide. The growth of iron silicide at 700°C is no longer two-dimensional, as at lower temperatures. Instead, three-dimensional nanometer size crystallites are formed on the bare Si 7 × 7 reconstructed surface. Their size, shape, and location on the surface substantially depend on the amount of the deposited material.

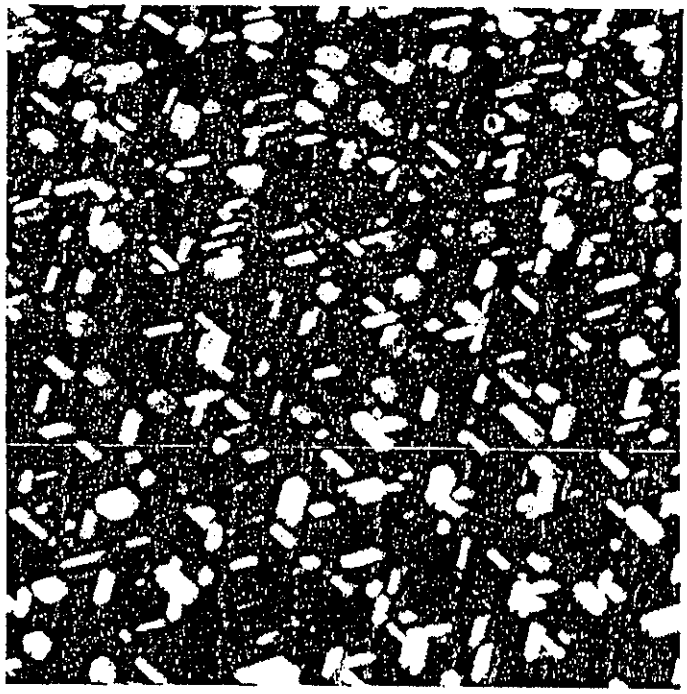

Fig. 5. Three-dimensional iron silicide crystallites grown upon deposition of 0.33 ML Fe and annealing at 700°C (scan size: 1 × 1 μm^2).

Crystallites formed upon 0.33 ML coverage are homogeneously distributed — their position on the surface is not affected by the edges of vicinal structure (Fig. 5). They nucleate both in the vicinity of the edges as well as in the centre of terraces. Prevailing number of crystallites have an elongated shape. The multitude of such forms may suggest that they are the initial stage of three-dimensional iron silicide crystallites at low Fe coverage regime. However, a certain amount of non-regular crystallites is also encountered. The long axes of crystallites clearly determine three directions, oriented every 60°, reflecting the symmetry of Si(111) 7 × 7 surface.

Figure 6 shows a high resolution STM image of a typical crystallite taken at a bias of −2.27 V. The edges of the base are parallel to [−110] directions of the unit mesh of the well reconstructed Si substrate. The length of the crystallite

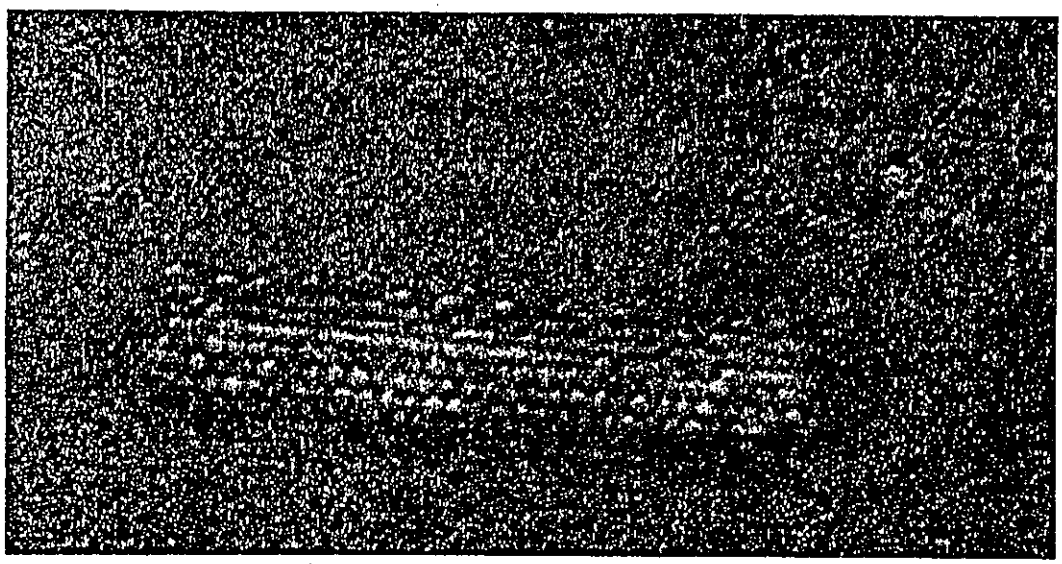

Fig. 6. Taken at -2.27 V, high resolution (20×40 nm^2) derivative image of a single iron silicide crystallite nucleated after deposition of 0.33 ML Fe and subsequent annealing at 700°C.

is about 250 Å. The topmost layer, three atomic rows in width, shows a (2×2) reconstruction with the distance between nearest neighbour atoms equal to 7.6 Å, which is expected both for CsCl- and CaF_2-type structure of iron silicide [2, 11, 27]. However, the excellent quality of the image allows finding that the crystallite consists of five monolayers, which in combination with its height equal to 7.9 Å reveals that it has a structure of CsCl-type. Various imaging of atoms in the topmost layer and on the facets, similar to that observed upon annealing at lower temperature (see Fig. 3a), as well as different apparent height of the crystallite measured at different biases, have a spectroscopic nature and will be discussed in the subsequent part of this paper.

Slightly different mechanism of crystallite growth at 700°C is found upon deposition of 2 ML of Fe (Fig. 7). The shape of truncated pyramid is dominating for this coverage. The elongated forms, typical of 0.33 ML coverage, are only sporadically met. Another striking feature is the strong influence of the vicinal structure on iron silicide crystallites nucleation. Crystallites grow mainly along the edges on the upper terraces. Practically none of them are found in the centre of terraces as it is observed for lower coverages. Such type of nucleation gives rise to the self-organization of iron silicide nanometer size crystallites, which may find practical implementation in nanoelectronics.

High-resolution image of a single crystallite grown upon deposition of 2 ML Fe and subsequent annealing at 700°C is depicted in Fig. 8. The very regular shape of a truncated pyramid with six facets of type alternatively: (100) and (111) is clearly visible. The topmost layer again displays, like in the case of lower coverage, a 2×2 reconstruction with the distance between nearest atoms equal to 7.6 Å. The edges of the base are oriented along [-110] directions of the very well

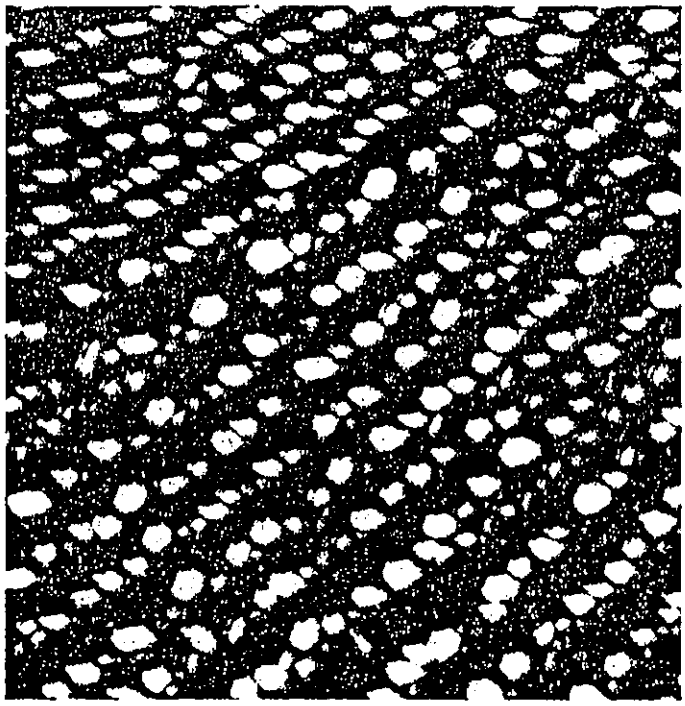

Fig. 7. Large scan (1×1 μm^2) image of the self-organized iron silicide crystallites grown on the Si(111) vicinal surface upon deposition of 2 ML Fe followed by annealing at 700°C.

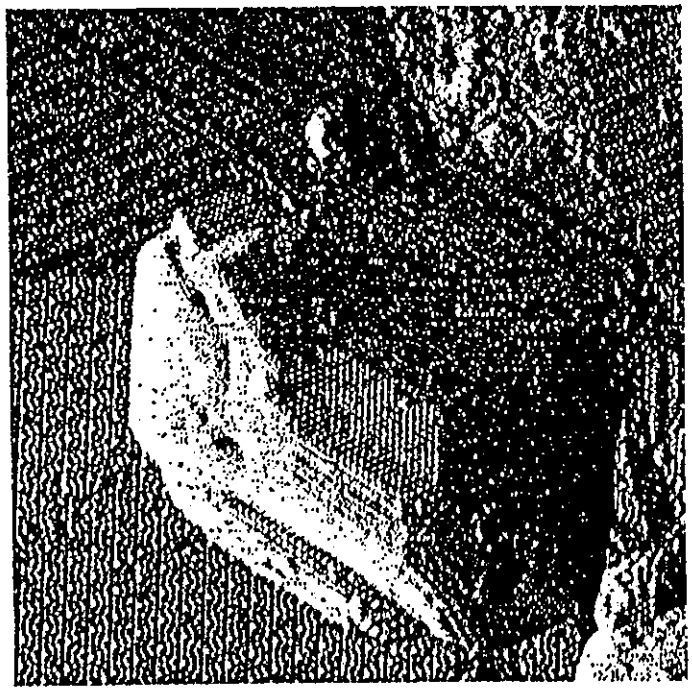

Fig. 8. STM derivative image of one of the elements of the self-organized array shown in Fig. 7.

reconstructed Si(111) 7 × 7 substrate. Such correlation between the orientation of grown crystallites and the unit meshes of the substrate for both coverages is evidence that three-dimensional crystallites of iron silicide grow epitaxially on the Si substrate. Measured height of the crystallite (68 Å) in combination with the number of atomic planes, estimated on the basis of the topography of one of the facets (more than 30), favours the CsCl-type structure.

The diffusion processes proceeding on the surface at 700°C are responsible for agglomeration of Fe atoms (partially observed upon annealing at 400°C), epitaxial growth of iron silicide crystallites and full reconstruction 7 × 7 of Si bare substrate, which is clearly visible in the background. It is reasonable to expect that all deposited Fe atoms are gathered in the volume of crystallized iron silicide. The temperature of 700°C is rather too low for re-evaporation of Fe atoms from the surface. The above assumption is taken into account in crystallite structure consideration in the subsequent part of the paper. The evidence of an intensive process of the Si surface etching, which supplies Si atoms for iron silicide formation, is very clear. The terraces of vicinal silicon surface have numerous, rounded edges corresponding to the height of double Si monolayer, which are not observed on the clean Si surface prior to the Fe deposition. In the vicinity of nucleated crystallites the substrate surface is flat without any dips around the crystallites. It means that the atoms necessary for iron silicide formation do not diffuse locally from sites in the vicinity of nucleating crystallites, but homogeneously from the entire surface. The localization of the big crystallites, grown upon deposition of 2 ML Fe, along the edges of the upper terrace may result from the fact that this site is energetically favoured to supply high amount of substrate material, necessary for crystallite growth.

As mentioned earlier, different imaging of surface atoms is ascribed to spectroscopic effects. This is a characteristic feature of both: flat reconstructed surfaces formed upon deposition of 2 ML Fe and subsequent annealing at 400°C as well as the surface and facets of iron silicide crystallites grown at 700°C. In the constant current mode the tip of STM does not follow the geometric profile of the surface, but also probes an electronic local structure and these two contributions cannot be easily separated. However, on the basis of spectroscopic effects and results reported in other works, it seems that the differentiation between Fe and Si atoms is becoming possible.

A prevailing number of studies reveal that due to the decrease in surface energy the topmost layer of iron silicide is Si terminated [11, 14, 20, 21, 28]. The Fe–Si bonding displays a homopolar nature, however in CsCl-type structure the transfer of approximately 0.5 electron charge per unit cell from Si atom to *d* orbital of Fe atom is observed [2]. Thus, taking into account the non-uniform distribution of A-type and B-type atoms depending on the terminating layer (which can be treated as a preliminary stage formation of three-dimensional iron silicide crystallites), the following explanation seems to be credible. As mentioned earlier, Si

atoms terminate the surface. They are very well distinguishable, because *sp* orbitals are better imaged by STM than *d* orbitals of Fe atoms. However these, which neighbour with Fe atoms in the layer underneath are slightly positively charged because of an electron transfer from Si towards Fe atom. When the occupied states are probed at negative bias of the tunneling junction, the intensity of the tunneling current decreases. In order to maintain a constant tunneling current, the STM tip approaches the surface and such type of surface atom is imaged as a "lower" one. Therefore the A-type atoms imaged as "lower" at negative bias are Si atoms adjacent to Fe atoms in subsurface layer whereas B-type ones are Si, which neighbour the same type of atoms underneath.

In order to study in detail the electronic structure of iron silicide crystallite surface, shown in Fig. 6, the measurements of the current imaging tunnelling spectroscopy (CITS) with atomic resolution have been performed. At positive bias the surface atoms are imaged in the same way. It is thus highly probable that the STM tip purely follows the topographic profile, i.e. the distance between the tip and the surface is kept constant over all atoms. In order to achieve the $I-V$ characteristics the bias of the tunneling junction has been swept from the positive to negative value. When the feedback loop is switched off to perform the spectroscopic measurements, the STM tip is positioned at the same height over the surface in every probed point. In such case the parameters of the junction barrier take the same values and the spatial variation of measured characteristics reflects merely electronic properties of the electrodes. Because the STM tip is cut from tungsten wire, which has a rather featureless electronic structure, the spatial variation, observed in current maps, should be associated only with the surface properties.

Constant current topography, simultaneously recorded current maps of the same area at various biases and $I-V$ as well as $\mathrm{d}I/\mathrm{d}V$ characteristics, measured at different sites of the surface are depicted in Fig. 9a–d. In topographic image (Fig. 9a) the bright vertical strip on the left side represents a part of the elongated iron silicide crystallite shown in Fig. 6. Very well reconstructed 7×7 surface of the bare Si is clearly seen in the background. In the current image recorded at 0.39 V (Fig. 9b) the area of crystallite is imaged in black (in the current maps larger intensity of tunneling current is imaged brighter). It means that the intensity of the current flowing through iron silicide to the silicon substrate is lower in comparison with that directly tunnelling to the substrate. Substantially different map was recorded at the negative bias of –1.1 V (Fig. 9c). The entire area of crystallite is imaged brighter than the uniform background of the bare silicon. Additionally the images of several surface atoms of crystallite are much brighter than the others. They correspond to the atoms, which are visible as "higher" ones in topography in Fig. 6. Approximately 25% of surface atoms of iron silicide crystallite display such a property. In accordance with the course of explanation given above, it is expected that the density of electronic states localized on such atoms takes a larger value.

In order to find the differences in electronic structure, atomically resolved spectroscopic characteristics were measured. Figure 9d depicts both $I-V$ and $\mathrm{d}I/\mathrm{d}V$ curves recorded at three various sites: bare silicon surface, bright and dark atoms of iron silicide crystallite. Each of them is averaged over at least ten runs obtained in various sites of the same type. As expected from the measurements of topography $I-V$ characteristics do not differ substantially in the range of positive biases. Merely for direct tunnelling to bare silicon the slope of the curve is higher

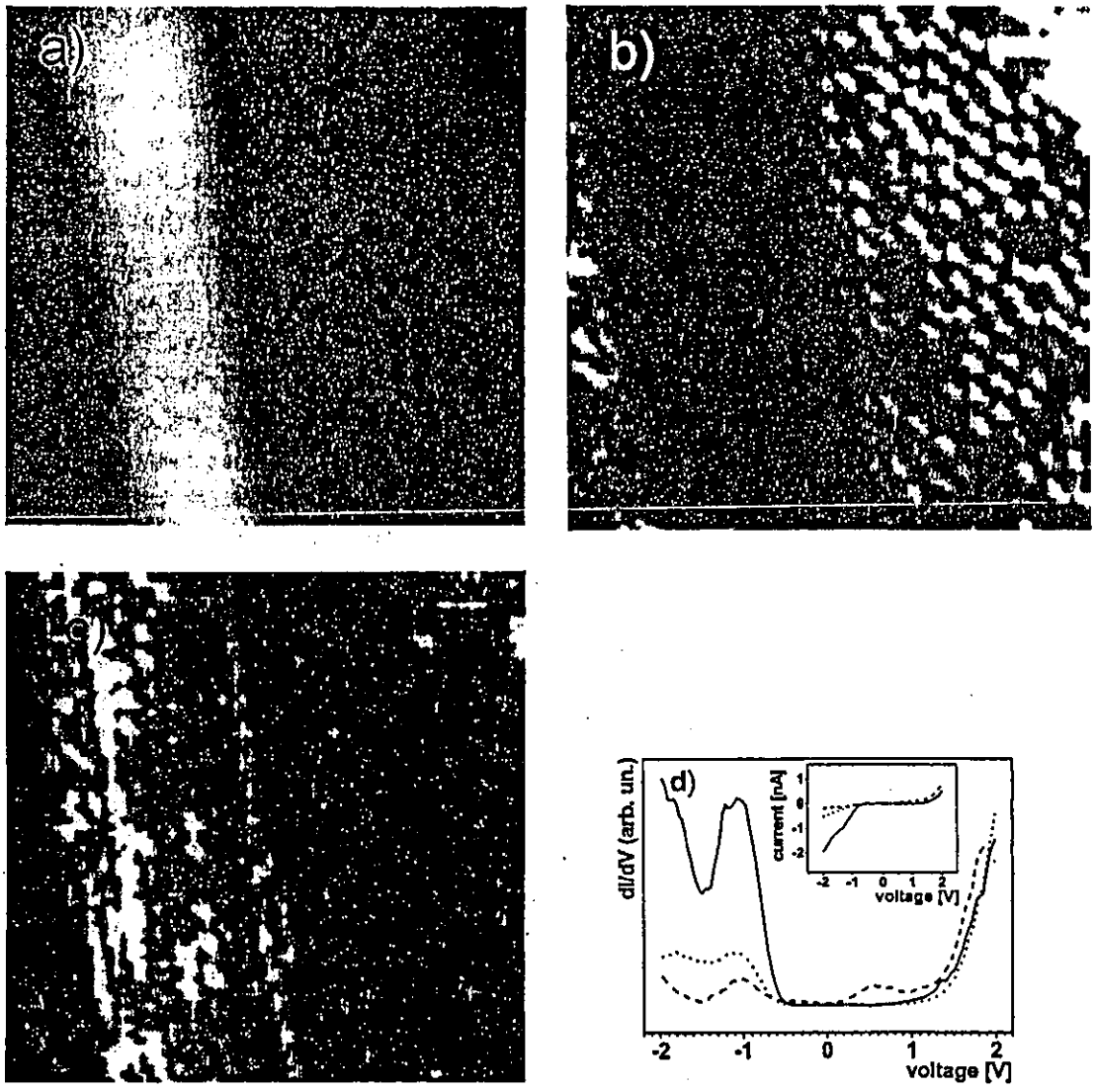

Fig. 9. (a) Recorded at +2.27 V STM topography image (15×15 nm^2) of the iron silicide nanocrystallite (bright vertical stripe on the left) grown on the bare Si(111) substrate after annealing of 0.33 ML Fe at 700°C. Current map (CITS) of the same area obtained at: (b) +0.39 V and (c) −1.1 V. (d) Averaged $\mathrm{d}I/\mathrm{d}V$ (in the insert $I-V$) characteristics recorded on: bare Si(111) surface (dashed line) and on iron silicide nanocrystal topmost layer: A-type atoms (dot line) and B-type atoms (solid line).

between 0.4 and 1.2 V. Much larger variations are observed below −0.7 V. Drastic increase in the tunnelling current is observed when the atoms of iron silicides, imaged in bright in the current map (Fig. 9c), are probed. The slope of $I-V$ characteristic for the remaining atoms of iron silicide crystallite is substantially lower, but still larger than that for pure silicon surface. Observed differences are emphasized in $\mathrm{d}I/\mathrm{d}V$ characteristics. Similarly to $I-V$ no differences are observed above 1 V. Below this bias $\mathrm{d}I/\mathrm{d}V$ curves measured on iron silicide crystallite are flat whereas for Si substrate there is an apparent peak at 0.6 V. The flat region, which may be associated with energy gap, extends down to −0.5 V for all curves. Below this bias, where the occupied states are probed, the curve measured on B-type atoms drastically arises and two very distinct peaks appear at −1.1 and −1.9 V. Much weaker increase is observed for A-type atoms as well as for Si surface. The shape of $\mathrm{d}I/\mathrm{d}V$ characteristic reflects, at least qualitatively, the dependence of density of states on energy. A higher peak observed for B-type atoms in comparison with A-type is associated with the regular filling of electron orbitals in Si atom on the surface, when it is adjacent to the same type in the layer underneath. In the opposite case the transfer of electron charge towards Fe atom depletes the filling of orbitals in the topmost Si atom, which results in a weaker increase in the tunneling current with the bias and lower intensity of the peak in $\mathrm{d}I/\mathrm{d}V$ characteristic. The conducting and valence bands for positive and negative bias, respectively, are clearly highlighted. Much wider — in comparison to Si — flat region around zero bias measured for iron silicide may suggest the presence of an additional tunneling barrier. Combination of the gathered data, i.e. metallic character of (CsCl)FeSi, diode-like drastic increase in the current intensity below −0.7 V ($I-V$ characteristics in Fig. 9d) and slightly larger apparent height of the same crystallite measured at negative bias in comparison with the height obtained at positive bias (e.g. from the profile comparison of the crystallite shown in Fig. 6), becomes consistent if the presence of the Schottky barrier at the interface between crystallites and n-type Si substrate is taken into account. Such an additional barrier reduces the tunnelling probability for the electrons flowing from the STM tip through the iron silicide crystallite to the substrate in comparison with the direct tunnelling to Si. The opposite bias decreases the efficiency of the barrier and tunnelling probability increases. In the constant current mode, in which topography is recorded, reduced tunnelling probability imposes the approach of the scanning tip over the surface, decreasing the apparent height of studied objects.

Detailed statistical analysis of the size of self-organized iron silicide crystallites grown on vicinal Si surface upon Fe deposition and subsequent annealing at 700°C enables an insight into their internal structure. The measured height, calibrated against the double Si monolayer step of 3.16 Å in height, reveals the quantization close to 1.5 Å, typical of CsCl-type structure. This is clearly illustrated in Fig. 6, which shows the image of crystallite of 7.9 Å in height consisting of five monoatomic layers. The height distribution in population of more than 80

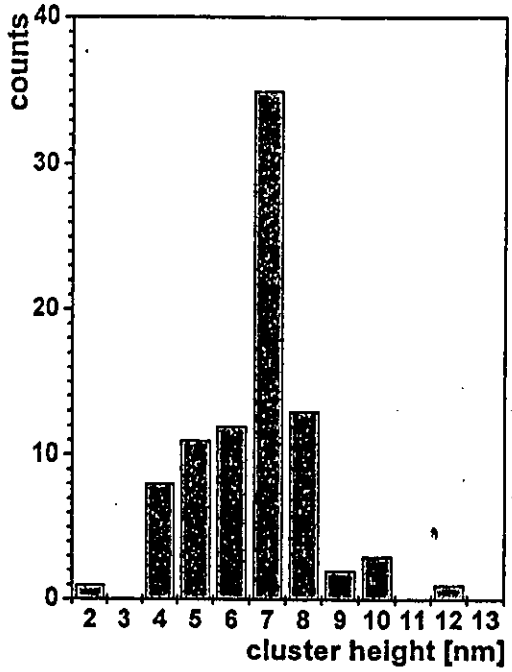

Fig. 10. Height histogram of iron silicide crystallites grown after annealing of 2 ML Fe at 700°C.

randomly selected crystallites grown upon deposition of 2 ML of Fe is shown in Fig. 10. Surprisingly, the obtained distribution has a non-Gaussian character. Instead, the crystallites of 7 nm in height dominate over the others, both larger and smaller in height. The above result may suggest that the investigated solid state reaction leads to the formation of a regular array of uniform in size iron silicide crystallites.

As mentioned earlier, the 2 × 2 reconstruction of iron silicide surface with the nearest neighbour distance between atoms equal to 7.6 Å is characteristic of both CsCl(FeSi) and γ-$FeSi_2$ phases. In order to identify the internal structure of grown crystallites, the ratio of their estimated volume to the volume of deposited iron is considered. The lattice parameter of CsCl-type phase is equal to 5.43 Å. The elementary cell of this phase contains eight atoms of Fe and Si. The lattice parameter of γ-$FeSi_2$ compound is comparable and equal to 5.39 Å, however the elementary cell consists of eight Si atoms and four Fe atoms. The CsCl vacancy type structure, in which the iron atoms are substituted by vacancies, is the intermediate one between the two phases described above. Under reasonable assumption that the temperature of 700°C is too low for re-evaporation of Fe atoms from the surface it is expected that all deposited Fe atoms are built in the iron silicide crystallites. Thus the ratio of compound volume to the bulk-like volume of deposited iron is equal to 1.7 and 3.3 for CsCl- and γ-type structures, respectively. The volume of grown crystallites may be approximately estimated on the basis of their height distribution and the fraction of the sample's area, which is covered with iron silicide. The statistics for both coverages are shown in Table. Obtained results

TABLE

Parameters applied for estimation of iron silicide crystallite structure.

Coverage [ML]	Fe layer thickness [nm]	Occupied surface [%]	Crystallite mean height [nm]	V_{FeSi}/V_{Fe}
0.33	0.048	11	0.8	1.83
2	0.29	13	6.6	2.9

clearly confirm that the grown iron silicide crystallites for both coverages have CsCl-type structure, however the smaller ones are more compact with composition close to 1:1, whereas in bigger ones a certain amount of vacancies is present. Inferred internal structure of crystallites coincides well with the STM images of their surface. In the case of smaller crystallites the different STM imaging of atoms is frequent, which is in contrast to bigger ones, where the surface atoms are imaged in the same way. It suggests that in smaller crystallites, where the contribution of atoms located on the surface and in subsurface layers is much higher and the fraction of Fe atoms approaches 50%, the presence of Fe atoms in the vicinity crystal surface is highly probable. The surface of big crystallites, in which the relative number of surface atoms is much lower, is probably terminated with a double Si layer, as predicted by theoretical models [14, 20], and in consequence imaged homogeneously.

4. Conclusions

The solid state reaction proceeding on Si vicinal surface upon deposition of Fe and subsequent annealing results in the growth of iron silicide crystallites. The initial stage of nucleation is found already upon annealing at 400°C. At 700°C metallic, three-dimensional iron silicide crystallites of CsCl-type structure grow in the form of truncated pyramids on bare 7×7 reconstructed Si surface. Depending of Fe coverage they take different shape, size, and location. The smaller are elongated and nucleate homogeneously on the surface. The bigger ones decorate the edges of the upper terraces giving rise to formation of a regular array of nanometer in size metallic dots on the semiconducting substrate. They show a tendency to grow in uniform size of 7 nm in height. Basing on spectroscopic effects, the composition and structure of the crystallites' surface is proposed. Statistical analysis reveals that in bigger crystallites the contribution of vacancies in CsCl-type structure is higher in comparison with smaller ones. The properties of the interface between metallic crystallite and semiconducting substrate resemble Schottky barrier behaviour.

Acknowledgments

This work was partially supported by the State Committee for Scientific Research under the project R-34.

References

[1] D. Leong, M. Harry, K.J. Reeson, K.P. Homewood, *Nature* **387**, 686 (1997).

[2] H. von Känel, K.A. Mäder, E. Müller, N. Onda, H. Sirringhaus, *Phys. Rev. B* **45**, 13807 (1992).

[3] H. Sirringhaus, N. Onda, E. Müller-Gubler, P. Müller, R. Stalder, H. von Känel, *Phys. Rev. B* **47**, 10567 (1993).

[4] C. Pirri, M.H. Tuilier, P. Wetzel, S. Hong, B. Bolmont, G. Gewinner, R. Cortès, O. Heckmann, H. von Känel, *Phys. Rev. B* **51**, 2302 (1995).

[5] K.L. Whiteaker, I.K. Robinson, C. Benson, D.M. Smilgies, N. Onda, H. von Känel, *Phys. Rev. B* **51**, 9715 (1995).

[6] M. Fanciulli, C. Rosenblad, G. Weyer, A. Svane, N.E. Christensen, H. von Känel, *Phys. Rev. Lett.* **75**, 1642 (1995).

[7] M. Fanciulli, G. Weyer, A. Svane, N.E. Christensen, H. von Känel, E. Müller, N. Onda, L. Miglio, F. Tavazza, M. Celino, *Phys. Rev. B* **59**, 3675 (1999).

[8] J.M. Gallego, J. Alvarez, J.J. Hinarejos, E.G. Michel, R. Miranda, *Surf. Sci.* **251-252**, 59 (1991).

[9] N. Motta, A. Sgarlata, G. Gaggiotti, F. Patella, A. Balzarotti, M. de Crescenzi, *Surf. Sci.* **284**, 257 (1993).

[10] J.H. Oh, S.K. Lee, K.P. Han, K.S. An, C.Y. Park, *Thin Solid Films* **341**, 160 (1999).

[11] A.L. Vazquez de Parga, J. de la Figuera, C. Ocal, R. Miranda, *Europhys. Lett.* **18**, 595 (1992).

[12] U. Kafader, M.H. Tuilier, C. Pirri, P. Wetzel, G. Gewinner, D. Blomont, O. Heckmann, D. Chandesris, H. Magnan, *Europhys. Lett.* **22**, 529 (1993).

[13] X. Wallart, J.P. Nys, C. Tételin, *Phys. Rev. B* **49**, 5714 (1994).

[14] A. Mascaraque, J. Avila, C. Teodorescu, M.C. Asensio, E.G. Michel, *Phys. Rev. B* **55**, R7315 (1997).

[15] N. Jedrecy, A. Waldhauer, M. Sauvage-Simkin, R. Pinchaux, Y. Zheng, *Phys. Rev. B* **49**, 4725 (1994).

[16] J.J. Hinarejos, G.R. Castro, P. Segovia, J. Alvarez, E.G. Michel, R. Miranda, A. Rodriguez-Marco, D. Sánchez-Portal, E. Artacho, F. Ynduráin, S.H. Yang, P. Ordejón, J.B. Adams, *Phys. Rev. B* **55**, R16065 (1997).

[17] Le Thanh Vinh, J. Chevrier, J. Derrien, *Phys. Rev. B* **46**, 15946 (1993).

[18] K.A. Mäder, H. von Känel, A. Baldereschi, *Phys. Rev. B* **48**, 4364 (1993).

[19] U. Starke, J. Schardt, W. Weiss, W. Meier, C. Polop, P.L. de Andres, K. Heinz, *Europhys. Lett.* **56**, 822 (2001).

[20] M. Sauvage-Simkin, N. Jedrecy, A. Waldhauer, R. Pinchaux, *Physica B* **198**, 48 (1994).

[21] U.K. Köhler, J.E. Demuth, R.J. Hamers, *Phys. Rev. Lett.* **60**, 2499 (1988).

[22] W. Raunau, H. Niehus, G. Comsa, *Surf. Sci. Lett.* **284**, L375 (1993).

[23] J. Junquera, R. Weht, P. Ordejón, *Surf. Sci.* **482-485**, 625 (2001).

[24] A. Wawro, unpublished.

[25] U. Starke, W. Weiss, M. Kutschera, R. Bandorf, K. Heinz, *J. Appl. Phys.* **91**, 6154 (2002).

[26] W. Raunau, H. Niehus, T. Schilling, G. Comsa, *Surf. Sci.* **286**, 203 (1993).

[27] J. Chevrier, V. Le Thanh, S. Nitsche, J. Derrien, *Appl. Surf. Sci.* **56-58**, 438 (1992).

[28] S.A. Chambers, S.B. Anderson, H.W. Chen, J.H. Weaver, *Phys. Rev. B* **34**, 913 (1986).

Molecular Simulation, Vol. 30 (13–15), 15 November–30 December 2004, pp. 929–933

Taylor & Francis
Taylor & Francis Group

Structure and Electronic Properties of Metal Di-(4-thiophenyl)-porphyrin

Y. KIKUCHI, R.V. BELOSLUDOV, H. BABA, A.A. FARAJIAN, H. MIZUSEKI* and Y. KAWAZOE

Institute for Materials Research, Tohoku University, Sendai 980-8577, Japan

(Received January 2004; In final form July 2004)

The geometry and electronic structures of metal 5, 15-di-(4-thiophenyl)-porphyrin (MDTP) have been investigated using first-principles calculations. Several metal atoms, including Cr, Mn, Fe, Co, Ni, Cu and Zn, have been selected. It has been found that the dihedral angle between porphyrin and thiophenyl planes is close to the perpendicular, which means that the π conjugation in whole MDTP molecules is broken. The most stable spin configurations of Cr, Mn, Fe, Co and NiDTPs are $S = 2$, 5/2, 1, 1/2 and 0, respectively. Analysis of metal 3d-orbital splitting in Zn and NiDTP have shown that in the case of NiDTP, the out-of-plane interaction between metal 3d-orbitals and π orbital of porphyrin is larger than that in the case of ZnDTP. The results suggest that the Ni metal will enhance the conductance of DTP because transport properties in molecular systems have strong relations to the molecular π orbital.

Keywords: Metal porphyrin; Transport properties; First-principles calculations; 3d-orbital splitting

INTRODUCTION

Recently, the research field of the molecular electronics has advanced significantly with many experiments that probe the behavior of small groups of molecules, such as scanning probe microscope (SPM) technology [1]. It will make it possible to construct a molecular wire, molecular rectifier and other functional devices using a finite number of self-assembled molecules or even just single molecules in the near future. The theoretical studies are also important part of the molecular electronics because they can directly propose and design novel nanodevices as well as enrich the experimental intuition. For example, molecular electronics dates back to the original theoretical work in which Aviram and Ratner revealed the possibility of an organic molecule functioning as a molecular rectifier [2].

Theoretical studies have been mainly dedicated to the understanding of conduction mechanisms through different molecular systems [3–4] and how the electronic structure of the molecule and the geometry of the molecule/metal interface affect the conduction characteristics [5–6]. The porphyrin molecule is one of the most promising candidates for future nanoelectronic devices because it can be used as a building block in complex molecular circuits. This is supported by a recent discovery that different porphyrin arrays having rigid geometric structure and stability in air [7]. Using such arrays it is possible to control the π orbital delocalization which is desirable for molecular wire applications. Moreover, such porphyrin polymers can be doped by different kind of metals that can increase the opportunity to use these polymers in spintronics.

In this paper, we investigate the structures and electronic properties of different metal-containing porphyrin molecules by using first-principles calculations. The influence of the different metal atoms on electronic transport through the porphyrin core has been also analyzed.

METHOD

In this study we consider a porphyrin molecule with two thiophenyl substituents at its right and left sides, respectively, because the thiol-type sulfur atom has widely been used as the alligator clip for the connection to Au electrodes. We examine the structure and electronic properties of both

*Corresponding author. Tel.: +81-22-215-2054. Fax: +81-22-215-2052. E-mail: mizuseki@imr.edu

ISSN 0892-7022 print/ISSN 1029-0435 online © 2004 Taylor & Francis Ltd
DOI: 10.1080/08927020412331298667

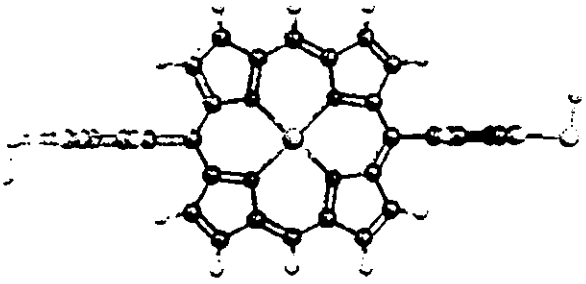

FIGURE 1 Structure of MDTP (M = Cr, Mn, Fe, Co, Ni, Cu, and Zn).

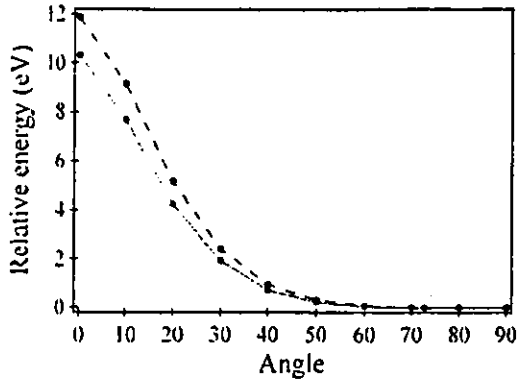

FIGURE 2 Relative energy of ZnDTP (solid) and ZnTPP (dashed) as a function of dihedral angle between porphyrin plane and thiophenyl groups.

undoped socalled free-based (FB), and metal-doped porphyrins (see Fig. 1). Seven first-row transition-metal complexes (from Cr to Zn) of 5,15-di-(4-thiophenyl)- porphyrin (MDTP), were selected for the investigation.

The geometry optimization of MDTPs has been performed by using density functional theory (DFT) coupled with B3LYP exchange-correlation functions. Moreover, the most stable spin configurations of MDTPs (M = Cr, Mn, Fe, Co, and Ni) have been examined and only the most stable spin configurations have been selected for the consideration. It is well-known that the density functional approximation (for example, BLYP) cannot reproduce the energy of excited state, and always gives the underestimated value as compared with the experimental one. The introduction of a hybrid functional in the DFT formalism gives a larger value as compared with a pure DFT one. Moreover, the B3LYP functional within the time-dependent DFT has been shown to produce low-lying excitation energies that are in excellent agreement with experimental results for porphyrins [8]. It has also been found that the optimization geometry of Zinc tetraphenylporphyrine (ZnTPP) better reproduces the experimental structure by B3LYP functional than by BLYP functional. We used the 6-311G and 6-31G(d) basis sets. The 6-311G basis set is commonly used for the prediction of the electronic structure of the first transition-row complexes, especially Fe [9], and therefore, it is mostly used in present study. For comparison, the 6-31G(d) basis set has been also applied in order to verify the obtained calculated results. All calculations were carried out using Gaussian 98 set of programs [10].

RESULTS AND DISCUSSION

First, we determined geometries of MDTPs. It has been found that the dihedral angle between the porphyrin ring and thiophenyl group is nearly perpendicular. Although it is well known that the phenyl ring at the meso-position prefers perpendicular conformation, the results for the thiophenyl group may be interesting from the experimental point of view, especially the energy difference between planar and perpendicular conformations. For instance, in order to gain accurate measurements of transport through these molecular structures, they should properly adsorb on metal contacts. Figure 2 shows the energy difference of ZnDTP as related to the most stable structure as a function of the rotation angle of the thiophenyl substituents. Moreover, the torsional potential of ZnTPP has been also calculated.

As expected, from this figure it is clear that the near-perpendicular conformation of meso-substituent is the most stable, while the planar conformation has the highest energy, with the energy difference about 10.3 eV. The energetically favorable perpendicular conformation leads to the destruction of the $\pi-\pi$ interaction between the porphyrin core and meso-substituents and thus to the reduction of the electron transport properties in this system. It is also interesting to note that there is no significant change in energy, when the torsion angle between meso-phenyl group and porphyrin core varied from 70° to 90°. In other words, the perpendicular conformation is flexible and can be easily changed to a near-perpendicular one under external perturbation such as temperature. The same tendency of change of torsional potential has been observed in ZnTPP (see Fig. 2). The only difference is in the value of relative energy, which is slightly higher than that in the case of ZnDTP, ranging from 0° to 60°. This can explain the dispersion of experimental data which reported near-perpendicular position of phenyl group with different absolute values of dihedral angle.

The geometry of the ZnTPP has been calculated using both B3LYP/6-311G and BLYP/6-31G(d) theory levels. The calculated Zn–N distance is found to be 2.047 and 2.061 Å using B3LYP and BLYP functionals, respectively. The obtained B3LYP result is more close to the experimental one (2.045 Å) [11] than that obtained by BLYP level. The optimized M–N bond lengths for the various MDTPs are collected in Table I

TABLE I Calculated and available experimental M–N bond lengths (Å) in MDTP

Stable spin configuration	*Present study B3LYP/6-311G*	*Experimental data*
CrDTP ($S = 2$)	2.045	–
MnDTP ($S = 5/2$)	2.087	–
FeDTP ($S = 1$)	1.999	1.972 [12]
CoDTP ($S = 1/2$)	1.986	1.949 [13]
NiDTP ($S = 0$)	1.971	1.930 [14]
CuDTP ($S = 1/2$)	2.016	1.981 [15]
ZnDTP ($S = 0$)	2.048	2.042 [15]

TABLE II Relative energy (eV) of MDTPs as calculated for the various spin states using B3LYP/6-311G and B3LYP/6-31G(d) (in parentheses) methods

	$S = 0$	$S = 1$	$S = 2$
CrDTP	2.84 (2.94)	1.97 (2.02)	0
FeDTP	1.53 (1.59)	0	0.21 (0.14)
NiDTP	0	0.51 (0.45)	–
	$S = 1/2$	$S = 3/2$	$S = 5/2$
MnDTP	0.97 (1.18)	0.16 (0.41)	0
CoDTP	0	0.20 (0.12)	–

Zero value indicates the energetically most stable spin configuration.

together with the experimental data for meso-tetraphenyl porphyrins (MTPP) [12–15]. The calculated M–N distances in CoDTP and NiDTP are close to 1.98 Å. That is, shorter than those in ZnDTP, MnDTP, and CrDTP, which are around 2.07 Å. The bonds between carbon and nitrogen atoms in pyrrole rings are practically the same for different MDTPs. The agreement between the calculated and available experimental data is quite good with the largest deviation of 0.04 Å. Accordingly, it is confirmed that the selected calculation method accurately predicts the structural properties of studied molecules.

The most stable spin configuration for each of MDTPs has been determined by the comparison of the total energy of optimized MDTP structures with the different spin configurations. At the first step, we have calculated the most stable spin configuration of FeTPP using B3LYP/6-311G level and compared with available theoretical and experimental data in order to make sure that the selected method can accurately predict the magnetic state of metal in metalporphyrin complexes. The most stable spin configuration of FeTPP has total spin $S = 1$. The state with $S = 2$ lies 0.51 eV above most stable spin configuration and in comparison with a magnetic susceptibility measurement that yielded a value of 0.62 eV [16]. The lowest closed-shell state ($S = 0$) lies 0.98 eV above the ground state. The recently obtained theoretical results are showed the same tendency magnetic configuration of FeTPP. The most stable spin configuration ($S = 1$) and the energy difference between this spin state and other configurations ($S = 2$ and $S = 0$) are found to be 0.75 and 1.15 eV, respectively [17].

Table II shows the difference in total energy for each of the spin configurations as related to the total energy of the most stable configuration defined as 0. Symbol S indicates the total spin of the system, which is the difference between the number of spin-up and spin-down electrons. CuDTP and ZnDTP have only one spin configuration, $S = 1/2$ and $S = 0$, respectively. In the cases of Cr, Mn, Fe, Co, and NiDTPs, the most stable spin configurations are $S = 2$, 5/2, 1, 1/2, and 0, respectively. These are in an agreement both with the theoretical [17] and experimental results [12,18,19] obtained for the metal-containing MTPP. The smaller energy difference between the lowest electronic configurations for the triplet and quintet states in FeDTP (0.21 eV) as compared to that in FeTPP (0.75 eV [17]), can be explained by the reduction of the molecular symmetry from D_{4h} in FeTPP to C_{2h} in FeDTP. It can be seen that both basis sets can predict the most stable spin configuration of different metalporphyrin complexes. However, in some cases (Fe and Co), the results obtained by 6-31G(d) show smaller energy differences between different spin configurations than that in the case of the 6-311G basis set. Therefore, the 6-311G basis set is more reliable to predict the spin configurations of Fe and CoDTP complexes.

The calculated large energy difference between the different spin configurations in the Mn, Fe, and Cr complexes suggest that these compounds can be used as a building blocks in the spintronic devices.

It is well known that the stronger the π orbital overlap in the system, the better its electron transport properties [2]. Thus, we investigated 3d-orbital splitting of different central metal atoms by porphyrin ligand field in order to understand the effect of out- and in-pane metal-ligand interactions on the conductance properties of MDTP. Theoretically, there are two possible 3d-orbital splitting by the square-planar ligand field. First, is an in-plane splitting scheme, which reflects a dominant in-plane interaction between the metal 3d($d_{x^2-y^2}$ and in part d_{z^2}) orbitals with porphyrin σ-donor orbitals. The second case is an out-of-plane splitting scheme, which reflects a dominant out-of-plane interaction between the metal 3d(d_{xz}, d_{yz}, d_{xy}) orbitals and π-donor or acceptor orbitals of the porphyrin ligand. Figure 3 shows the 3d orbital order for both cases.

Table III and IV show 3d-metal orbital splitting, in the case of ZnDTP and NiDTP complexes, respectively. Both of these structures have zero-spin configurations but the interactions between these metals and porphyrin ligand are different.

From these tables it has been seen that the 3d-orbital splitting has predominantly in-plane

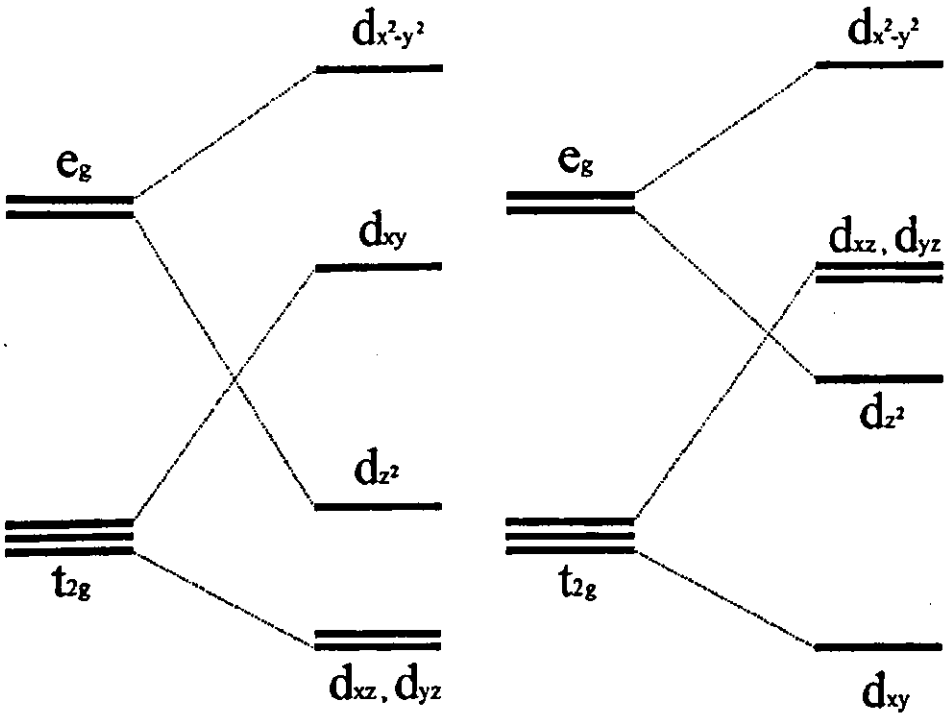

FIGURE 3 Schematic diagram of 3d metal orbital splitting in the square-planar ligand field: (a) in-plane and (b) out-of-plane.

character in the case of ZnDTP, while it is predominantly out-of-plane splitting in the case of NiDTP. Thus Zn has strong σ-type interactions with the porphyrin core, while Ni has strong π-type interactions with the porphyrin core. Moreover, the orbitals close to the HOMO–LUMO gap play a main role in conductance properties through the molecule. The analysis of the electronic structure shows that the predominantly metal-centred occupied molecular orbitals are shifted to the lower energy in the MO diagram. Thus, in the case of ZnDTP, the orbitals with metal contribution lie lower than in the case of NiDTP. In the case of NiDTP, the $d_{x^2-y^2}$ is unoccupied orbital (LUMO + 2) while d_π and d_{z^2} are close to HOMO (see Table IV). Moreover, the absence of electron in $d_{x^2-y^2}$ orbital results in shorter distance between Ni and N and therefore the better overlap between the orbitals of porphyrin ring is larger in this case as compared to the ZnDTP, where all the 3d orbitals of metal are filled. All of these results can verify that the expected conductance of NiDTP should be larger than that in ZnDTP.

SUMMARY

In this paper the structural and electronic properties of various MDTPs (M = Cr, Mn, Fe, Co, Ni, Cu, and Zn) were studied by using the DFT method. It was found that the stable structure of MDTP has near perpendicular dihedral angle between porphyrin and thiophenyl planes. The most stable spin states for Cr, Mn, Fe, Co, and NiDTPs are $S = 2$, 5/2, 1, 1/2, and 0, respectively. The analysis of 3d-orbital splitting shows that different metal atoms have different contributions in π out-of-plane orbitals. The results imply that incorporation of the Ni into the porphyrin may enhance the transport properties larger than incorporation of the Zn. Moreover, the thyophenyl groups conformation leads to the elimination of the π conjugation in whole MDTP structures and other connections of porphyrin to electrodes should be proposed in order to realize the molecular wire for the interconnections between electronic devices.

TABLE III 3d-metal orbital splitting of ZnDTP

Molecular orbital	*3d-metal orbital*	*Energy level (eV)*
HOMO-2	$d_{x^2-y^2}$	−6.69
HOMO-24	d_{xy}	−10.32
HOMO-25	d_{z^2}	−10.50
HOMO-34	d_{yz}	−11.22
HOMO-35	d_{xz}	−11.28

TABLE IV 3d-metal orbital splitting of NiDTP

Molecular orbital	*3d-metal orbital*	*Energy level (eV)*
LUMO + 2	$d_{x^2-y^2}$	−1.61
HOMO-2	d_{yz}	−6.22
HOMO-3	d_{xz}	−6.24
HOMO-4	d_{z^2}	−6.33
HOMO-17	d_{xy}	−8.10

Acknowledgements

The authors would like to express their sincere thanks to the staff of the Center for Computational Materials Science of the Institute for Materials Research, Tohoku University for their continuous support of the SR8000 supercomputing facilities. This study was performed through Special Coordination Funds for Promoting Science and Technology from the Ministry of Education, Culture, Sports, Science and Technology of the Japanese Government.

References

[1] Joachim, C., Gimzewski, J.K. and Aviram, A. (2000) "Electronics using hybrid-molecular and mono-molecular devices", *Nature* **408**, 541.
[2] Aviram, A. and Ratner, M.A. (1974) "Molecular rectifier", *Chem. Phys. Lett.* **29**, 277.
[3] Park, J., Pasupathy, A.N., Goldsmith, J.I., Chang, C., Yaish, Y., Petta, J.R., Rinkoski, M., Sethna, J.P., Abrun, H.D., McEuen, P.L. and Ralph, D.C. (2002) "Coulomb blockade and the Kondo effect in single-atom transistors", *Nature* **417**, 722.
[4] Di Venta, M., Pantelides, S.T. and Lang, N.D. (2000) "First-principles calculation of transport properties of a molecular device", *Phys. Rev. Lett.* **84**, 979.
[5] Majumder, C., Mizuseki, H. and Kawazoe, Y. (2001) "Molecular scale rectifier:theoretical study", *J. Phys. Chem. A* **105**, 9454.
[6] Majumder, C., Briere, T.M., Mizuseki, H. and Kawazoe, Y. (2003) "Thiophene thiol on the Au(111) surface: sizedependent absorption study", *J. Chem. Phys.* **118**, 9809.
[7] Tsukada, A. and Osuka, A. (2001) "Fully conjugated porphyrin tapes with electronic absorption bands that reach into infrared", *Science* **293**, 79.
[8] Nguyen, K.A., Day, P.N. and Pachter, P. (1999) "Effects of halogenation on the ionized and excited states of free-base and zinc porphyrins", *J. Chem. Phys.* **110**, 9135.
[9] Nemykin, V.N., Kobayashi, N., Chernii, V.Y. and Belsky, V.K. (2001) "Mossbauer, crystallographic, and density functional theoretical investigation of the electronic structure of bis-ligated low-spin iron(II) phthalocyanines", *Eur. J. Inorg. Chem.* **3**, 733.
[10] Frisch, M.J., *et al.* (1998) *Gaussian 98*, revision A. 1 (Gaussian, Inc., Pittsburgh, PA).
[11] Scheidt, V.R., Mondal, J.U., Eigenbrot, C.W., Adler, A., Radonovich, L.J. and Hoard, J.L. (1986) "Crystal and molecular structure of the silver(II) and Zn(II) derivatives of meso-tetraphenylporphyrin. An exploration of crystal-packing effects on bond distance", *Inorg. Chem.* **25**, 795.
[12] Collman, J.P., Hoard, J.L., Kim, N., Lang, G. and Reed, C.A. (1975) "Synthesis, stereochemistry and structure-related properties of $\alpha,\beta,\gamma,\delta$-tetraphenylporphinatoiron(II)", *J. Am. Chem. Soc.* **97**, 2676.
[13] Madura, P. and Scheidt, W.R. (1976) "Stereochemistry of low-spin co-porphyrins 8. $\alpha,\beta,\gamma,\delta$-tetraphenylporphinatocobalt(II)", *Inorg. Chem.* **15**, 3182.
[14] Maclean, A.L., Foran, G.J., Kennedy, B.J., Turner, P. and Hambley, T.W. (1996) "Structural characterization of nickel(II) tetraphenylporphyrin", *Aust. J. Chem.* **49**, 1273.
[15] Fleischer, E.B., Miller, C.K. and Webb, L.E. (1964) "Crystal and molecular structures of some metal tetraphenylporphines", *J. Am. Chem. Soc.* **86**, 2342.
[16] Boyd, P.D.W., Buckingham, A.D., McMecking, R.F. and Mitra, S. (1979) "Paramagnetic anisotropy. Average magnetic-susceptipility, and electronic-structure of intermediate-spin $S = 1$ (5,10,15,20-tetraphenylporphyrin)iron(II)", *Inorg. Chem.* **18**, 3585.
[17] Liao, M.-S. and Scheiner, S. (2002) "Electronic structure and bonding in metal porphyrins, metal = Fe, Co, Ni, Cu, Zn", *J. Chem. Phys.* **117**, 205.
[18] Lin, W.C. (1976) "D-orbital energies and low-lying excited-states of cobalt porphyrins", *Inorg. Chem.* **15**, 1114.
[19] Subramanian, J. (1975) *Porphyrins and Metalloporphyrins* (Elsevier Scientific, Amsterdam), p 555.

ELSEVIER

Science and Technology of Advanced Materials 4 (2003) 377–382

SCIENCE AND TECHNOLOGY OF ADVANCED MATERIALS

www.elsevier.com/locate/stam

Molecular orbital analysis of frontier orbitals for molecular electronics: a case study of unimolecular rectifier and photovoltaic cell

Hiroshi Mizuseki[a,*], Rodion V. Belosludov[a], Amir A. Farajian[a], Nobuaki Igarashi[a], Jian-Tao Wang[a,b], Hao Chen[a,c], Chiranjib Majumder[a,d], Shigeyuki Miura[a], Yoshiyuki Kawazoe[a]

[a]*Institute for Materials Research, Tohoku University, 2-1-1 Katahira, Aoba-ku, Sendai, Miyagi 980-8577, Japan*
[b]*Institute of Physics, Chinese Academy of Sciences, Beijing 100080, China*
[c]*Physics Department, Fudan University, Shanghai 200433, China*
[d]*Novel Materials and Structural Chemistry Division, Bhabha Atomic Research Center, Mumbai 400 085, India*

Received 7 May 2003; revised 16 June 2003; accepted 25 June 2003

Abstract

Recently, unimolecular devices have attracted significant attention as a 'post-silicon technology' to enable the fabrication of future nanoscale electronic devices. In this paper, we describe a candidate molecule for a rectifier function using porphyrin polymer and a photovoltaic cell using fullerene-based supramolecule. We have investigated the geometric and electronic structure of these organic molecules using an ab initio quantum mechanical calculation. These results for the porphyrin polymers show that the localization of the unoccupied orbital state on the acceptor moiety mostly depends on their structures. The calculated results for the electronic structure of a naphthalocyanine–fullerene supramolecule manifest that the HOMO's were localized on the donor sub-unit and the LUMO's were localized on the acceptor sub-unit.

Keywords: Molecular device; Molecular rectifier; Nanotechnology; Nanoelectronics; First-principles calculations; Photovoltaic cell

1. Introduction

For many years, progress in microelectronics has been associated with the reduction of the minimum feature size of integrated circuits. However, this trend, described by Moore's law, seems to be ending due to process and physical limitations. The minimum device feature size is now approaching dimensions comparable with atomic and molecular sizes. In other words, 'silicon technology' has an intrinsic limitation in the near feature. To overcome this situation, the field of molecular electronics has attracted much attention as a 'post-silicon technology.' A quarter of a century ago, Aviram and Ratner [1] first demonstrated how an organic molecule could function as a molecular device. Recently, this work has been further supported by a number of experimental results [2–6] and several theoretical studies have been published [7–13]. Nevertheless, the question regarding the properties of a relatively simple molecule and molecular systems remains unsettled, because the lack of suitable and effective technologies for measuring the conductance properties of an individual molecule, for example, the manipulation of a unimolecule and establishment of an electrical contacts.

Computer simulation a is useful tool in the field of molecular electronics, as the stable and electrical structures of a unimolecule are unknown and cannot be studied in detail by experiment. Our Institute has covered a wide range of molecular systems which have potential application in molecular electronics using first-principles calculations with a collaboration of experimental groups; molecular rectifiers [14–16], molecular enamel wires (covered wires) [17–19], molecular switches [20], molecular resonant tunneling diodes [21,22], molecular logic [23], connection between polymers and metal electrodes [24,25], Sb line on Si(001) [26], electronic transport though small molecules [27–29], bent carbon nanotubes [30], etc. In this paper, we present out recent investigations related to molecular electronics, using ab initio methods. All the calculations were performed using the GAUSSIAN98 program [31].

* Corresponding author. Tel.: +81-22-215-2054; fax: +81-22-215-2052.
E-mail address: mizuseki@imr.edu (H. Mizuseki).

1468-6996/$ - see front matter © 2003 Elsevier Ltd. All rights reserved.
doi:10.1016/S1468-6996(03)00061-5